CrossMark

ORIGINAL ARTICLE

Automatic optic disk detection in retinal images using hybrid vessel phase portrait analysis

Nittaya Muangnak[1] · Pakinee Aimmanee[1] · Stanislav Makhanov[1]

Abstract We propose *vessel vector-based phase portrait analysis* (VVPPA) and a hybrid between VVPPA and a clustering method proposed earlier for automatic optic disk (OD) detection called the *vessel transform* (VT). The algorithms are based primarily on the location and direction of retinal blood vessels and work equally well on fine and poor quality images. To localize the OD, the direction vectors derived from the vessel network are constructed, and points of convergence of the resulting vector field are examined by phase portrait analysis. The hybrid method (HM) uses a set of rules acquired from the decision model to alternate the use of VVPPA and VT. To identify the OD contour, the scale space (SS) approach is integrated with VVPPA, HM, and the circular approximation (SSVVPPAC and SSHMC). We test the proposed combination against state-of-the-art OD detection methods. The results show that the proposed algorithms outperform the benchmark methods, especially on poor quality images. Specifically, the HM gets the highest accuracy of 98% for localization of the OD regardless of the image quality. Testing the segmentation routines SSVVPPAC and SSHMC against the conventional methods shows that SSHMC performs better than the existing methods, achieving the highest PPV of 71.81% and the highest sensitivity of 70.67% for poor quality images. Furthermore, the HM can supplement practically any segmentation model as long as it offers multiple OD candidates. In order to prove this claim, we test the efficiency of the HM in detecting retinal abnormalities in a real clinical setting. The images have been obtained by *portable lens connected to a smart phone*. In detecting the abnormalities related to diabetic retinopathy (DR), the algorithm provided 94.67 and 98.13% for true negatives and true positives, respectively.

1 Introduction

One in ten of the patients with diabetes has a high risk of developing diabetic retinopathy (DR) [1]. Therefore, they are suggested to attend an annual clinical checkup. Early screening of eye diseases by ophthalmologists can help patients having diabetes to receive proper treatment at an early stage. Astonishingly, according to the statistics provided by the World Health Organization (WHO), the number of people across the world with diabetes has risen very rapidly from 108 million in 1980 to 422 million in 2014 [2]. This implies the necessity of automatic screening systems to assist ophthalmologists in diagnosing early stages of ophthalmic conditions such as glaucoma, DR, or age-related macular degeneration [3] using computer-assisted diagnostics. Since eye fundus imaging is a frequent clinical procedure, the retinal fundus images are commonly used for a preliminary diagnosis and detection of suspicious cases.

The optic disk (OD) is one of the crucial points in a retina. It is important for establishing a reference frame for other regions of clinical importance such as the fovea or macula and to diagnose the abnormalities. The OD usually appears in healthy retinal images as a bright, yellowish, circular, or oval object, roughly one sixth the width of the image in diameter [4], which is partly entered by optic nerves. Any irregularity in the appearance

✉ Pakinee Aimmanee
  pakinee@siit.tu.ac.th

[1] Sirindhorn International Institute of Technology, Thammasat University, 131 Moo 5, Tiwanont Road, Bangkadi, Muang, Pathum Thani 12000, Thailand

🍂 Springer

of the OD is a sign of abnormalities or diseases such as glaucoma, DR, or hypertensive retinopathy [5].

Conventional OD detection algorithms usually rely on the assumption that the OD appears in a central position as a bright and circular object of a certain size, characterized by a certain variation of the gray level (entropy). Various researchers have attempted to identify the OD center as the largest cluster of bright pixels. The existing methods report a success rate up to 100%. Similar ideas are exploited by template-matching-based techniques [6–8].

A survey on the recent literature by Winder et al. [9] cited 38 papers on OD localization and segmentation. In particular, principal component analysis, active contour models (snakes), watershed transforms, and their combination were proposed in [10–13]. Other models include algorithms based on intensity variation [14], Hough transform/fuzzy hybrid neural network [15], a template-based approach combined with morphological operations [16], and the curvelet transform [17–19].

Pereira et al. [20] analyzed the presence of brightness on a series of blurred images and applied an ant colony optimization algorithm and anisotropic diffusion. OD localization based on an approximate nearest neighbor field was proposed by Ramakanth and Babu [21]. Sopharak et al. [22] apply a two-class Bayesian classifier and mathematical morphology. The circular Hough transform was proposed by Azuara-Blanco et al. [23]. However, Zhu et al. [24] showed that the performance of the method could be very poor even when the shape was only slightly non-circular.

One of the most efficient algorithms successfully tested against many existing methods is proposed by Lu [25]. The modification of the circular transform (CT) combined with evaluation of the brightness has been proven to be more efficient, more accurate, and faster than other state-of-the-art methods such as the morphological approach proposed by Welfer et al. [26], a vessel's direction-matched filter proposed by Youssif et al. [27], localization using dimensionality reduction of the search space proposed by Mahfouz and Fahmy [28], genetic algorithms proposed by Carmona et al. [29], and the local refinement active contour model by Giachetti et al. [30]. Lu's method, first, localizes the OD based on a probability map constructed from the image gradient and intensity in the horizontal and vertical directions. The circular transformation is applied next, to detect the shape of the OD. An accuracy of about 98.77% is reported (considerably higher than the competing methods).

However, a major drawback of the feature-based approaches including CT of Lu (CTL) is that on poor quality images the method may generate multiple false ODs. Moreover, in these cases, physical appearance such as shape, color, brightness, or size of the actual OD becomes abnormal. An OD obscured by blood vessels or only partially visible (blur, shadows, noise) could be totally misclassified. Besides, precise OD identification based on the abovementioned features could be sensitive to pathologies such as white/yellow lesions, exudates, or bright artifacts appearing on the retinal photographs [31].

Another important subclass of the detection algorithms is based on the convergence of the vascular network to the OD. However, only a few existing methods exploit this feature. Akita and Kuga [32] traced the parent-child relationship between blood vessel segments, tracking back to the center of the OD. Chrastek et al. [33] checked the area where vertically oriented vessels converge as a single line of infinite length. Consequently, the detection of the convergence area was reduced to the line intersection problem.

The least square polynomial curve fitting algorithm and multi-level thresholding technique were applied by Kavitha and Devi [34] to localize the OD by detecting the strongest convergence point of blood vessels. A geometrical parametric model was proposed by Foracchia et al. [35] using the parabolic approximation of the vascular network to describe the general direction of retinal vessels at any given position in the image. The vessel directions were parameterized and the simulated optimization was used to obtain the coordinates of the center of the OD.

Niemeijer et al. [36] applied a k-nearest neighbor regression and a circular template on all vessel pixels to locate the OD. Proposed by Dehghani et al. [37], the OD was identified by finding the region having the highest density of vessels, corners, and bifurcation points using Harris corner detection. This algorithm was effective under invariance of rotation of retinal images, whereas the presence of pathological regions needed to be distinguished, and the desired OD contour required high variance contrast between OD and the surrounding background.

Welfer et al. [26] and Zhang and Zhao [38] used the assumption that the major vessels line up horizontally. The major drawback of these approaches is that they are not rotationally invariant. Vascular networks and intensity information were combined to examine the entropy of vascular directions in Mendonca et al. [39]. The distribution of vessel orientations around an image point is quantified using the entropy of vascular directions. The OD localization is done by searching for the high intensity image area that has maximal values of entropy. The active contour (snake) was employed by Semashko et al. [40]. The positions of the vessels were used to correct the pressure force of the active contour to improve the convergence of the snake to the OD center.

Rangayyan et al. [41] used Gabor filters to detect vessels to produce the orientation field. The resulting vector field was analyzed by the phase portrait analysis (PPA) to detect the points of convergence. The method reported an accuracy up to 100% on the DRIVE database [42]; however, the method failed when applied to poor quality images from STARE [43] (69.1%). The main reason for that is that the vessels extracted from the poor quality images usually create an inappropriate vector field. Consequently, the PPA generates multiple convergence points and a false OD.

In this paper, we show that a proper vector field can be generated using a certain set of features at the bifurcation points. These features (rather than the direction of blood vessels) combined with some additional vectors allow us to process poor quality images. For instance, the accuracy of the PPA on STARE has been increased to 99% with the reference to [43].

Another outstanding vessel convergence technique was introduced by Hoover and Goldbaum [4]. The method, called fuzzy convergence (FC), creates a fuzzy segment of which an area was provided by a voting scheme for corresponding pixels of each segmented vessel. An image map, representing the strong points of the convergence, was calculated by summation of votes. The map was then smoothed and the strongest convergence points are detected by thresholding. The FC technique was combined with a feature-based approach, which employs illumination equalization to minimize the large intensity variation at different scales. Testing on the STARE database showed acceptable performance overall (89%) and full success on the healthy retina images (100%). Nevertheless, the hierarchical structure of the retinal vessels and their importance were not considered. The retinal vessel network consists of both skeletonized primary and secondary attributes to the optic nerve head. The main vessels converge to the OD, whereas the secondary vessels are positioned randomly.

The most recent approaches include gravitational law-based method proposed by Alshayeji et al. [44], a variety of AI-based methods such as the firefly algorithm by Rahebi and Hardalac [45], ant colony optimization by Pereira et al. [20], and convolutional neural network developed by Tan et al. [46].

Other approaches include ensemble-based framework by Harangi and Hajdu [47], morphological approach [26], active contours [13, 48, 49], and parabolic approximation by Wu et al. [50]. A feature-based approach for pathological images has been proposed by Xiong and Li [51]. The algorithm employs a confidence score derived from vessel direction, intensity, OD edges, and size of the bright region. Parallel software for the localization of the OD in retinal fundus color images has been implemented with the graphics processing units in Díaz-Pernil et al. [52]. Wavelets, mathematical morphology, and Hessian-based multi-scale filtering are used in Rodrigues and Marengoni [53]. An equiripple low-pass finite impulse response filter to suppress the response of the blood vessels and detect the OD has been designed in Bharkad [54]. A global vessel symmetry component count and local vessel symmetry inside the OD region were used in Panda et al. [55].

However, only a few algorithms use the structure and the *direction* of the vessel network, which is an important feature in case of poor quality images.

In this paper, we use the fact that the geometry of the vessels converging at bifurcations indicates the direction to the OD. In order to find these directions, the smallest branching angle is evaluated at each bifurcation. We assume that the "main" vessel directed to the OD is opposite to the smallest branching angle. This assumption is not always correct when we consider pathological cases comprising individual fuzzy and distorted blood vessels. However, for the majority of the images (even the poor quality images), the smallest bifurcation angle points in the correct direction. Moreover, in order to define the main vessel, we consider not only the branching angle but also several selected features as well, i.e., thickness, tortuosity, and intensity.

In order to improve the quality of the resulting vector field, sole vessels are also taken into account, based on their importance. Besides, the bifurcation vectors have been supplemented by the so-called Mahfouz's vectors [28] derived from the observation that the vessels are positioned predominately along the vertical direction.

Our new technique is based on interpolation of the above representative vectors throughout the entire image and analyzing the resulting vector field by phase portrait analysis (VVPPA). The VVPPA approach is combined with the vessel transform (VT) [56], based on clustering the vessels into the binary trees and using a decision rule-based method. The combination of VVPPA and VT is called the hybrid method (HM). The HM is integrated into the SS analysis proposed in [57].

The novelty of the method is the use of the PPA applied to the interpolated vector field constructed from the bifurcation points, Mahfouz's vectors, sole vessel vectors (SVV), and the bouncing vectors (BV) (*See* the next section). The vectors are selected by using an advanced SVM and decision tree models. The method combines the PPA and VT. The combination is also based on the decision tree, which includes several specific vessel-based features.

The new algorithm has been tested on fair and poor quality retinal images from two databases (172 images) against the FC method [4], a recent modification of the CT [25], and the VT [56] applied without the hybridization with VVPPA. Furthermore, the SS boundary detection [57] was tested with and without the VVPPA and the HM. The numerical experiments demonstrate that the proposed algorithms outperform the baseline methods in terms of the precise localization of the OD and the accuracy of segmentation in the framework of the SS scheme. Finally, we test the efficiency of the HM in detecting retinal abnormalities in a real clinical setting (182 images). The images have been obtained by portable lens connected to a smart phone.

2 Hybrid OD detection method

2.1 OD localization

In this section, we present *vessel vector-based phase portrait analysis approach* (VVPPA) and a HM comprising VVPPA and VT.

2.1.1 Vessel vector-based phase portrait analysis approach

Five types of vectors are defined in the framework of VVPPA, namely

1) The shifted leading bifurcation vectors (SLBV)
2) The SVV
3) The Mahfouz vectors (MV)
4) The BV
5) The interpolated vectors

The SLBV are constructed by considering *bifurcations* consisting of three vessels. A circle centered at a junction is drawn and the intersection points of the circle with the vessels are marked. Normalized vectors from the junction to the intersection *are the bifurcation vectors* (Fig. 1). Next, the leading vectors are selected from the bifurcation vectors using the opposite angle, tortuosity, thickness, and contrast. The opposite angle of a vector is an angle between the other two vectors originated from the same bifurcation point. Tortuosity is the ratio of the distance to the displacement of two end points of the vessel segment. Thickness is the average width of the vessel segment considered from the bifurcation point to the intersection point. Contrast is the difference of the cumulative intensity between the vessel segments and their surrounding background from the bifurcation point to the intersection point. The angle, tortuosity, thickness, and contrast are normalized. The classification is based on the SVM method [58] applied using training and testing sets. The rules obtained from the training set are applied to the testing collection. Once the leading vector is obtained, we shift it along its direction to the end of the corresponding vessel (*See* Fig. 1). Usually, this step improves the OD detection.

The SVV are often the main vessels. Therefore, they contribute useful information about the OD location. To generate the SVV, we select the sole vessels, which are not too short, not too thin, and not too faint using a threshold selection technique. For each SV, we randomly pick a direction and normalize the resulting vector. The directions of the SVV are to be corrected later by the VVPPA. Furthermore, the OD approximation proposed by Mahfouz and Fahmy [28] is based on an observation that the retinal arteries and veins emerge from the OD mainly in the vertical direction and then progressively branch into main horizontal vessels. Thus, the *x*-location of the OD yields the greatest difference between the vertical and horizontal edges. Further, we consider a window with the length equal to the average diameter of the OD moving in the horizontal direction. The window containing the largest number of bright pixels defines the *y*-location of the OD. The four corresponding MV are shown in Fig. 2.

The Mahfouz's approach is experimentally proven to be fairly efficient with up to 92.6% accuracy [28]. It usually works well when the vessel structure is complete and the OD is clear. We thus employ MV to be a part of the proposed
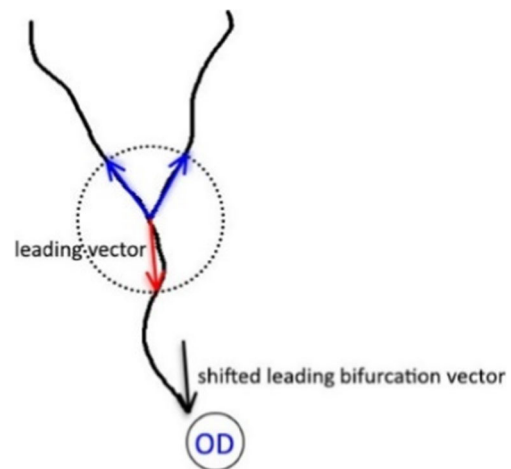

Fig. 1 An illustration of how a shifted leading bifurcation vector is obtained

algorithm. When the quality of the image is poor, the Mahfouz's approach may not yield a good accuracy. Nevertheless, in many cases, the MVs contribute to the accuracy of the HM.

The BV are created with the purpose to improve the convergence of PPA. A bouncing vector of a vector V is a unit vector starting at the edge of retinal image and pointing opposite to V. In this work, the BV are derived from SLBV, SVV, and MV.

Finally, the interpolated vectors are constructed at every grid point of the retinal image using triangulation of the image and linear interpolation. The PPA assumes that the vector flow v changes linearly in the neighborhood of the critical point as follows, $v = Ap$, where $p = (x, y)$ is the Cartesian coordinate and A the corresponding matrix. The matrix is approximated by the least square method applied to v in the moving window centered at p. The flow patterns characterized by the eigenvalues of matrix A are shown in Table 1, where λ_i are the eigenvalues, $R_i = Re\lambda_i$, $I_i = Im\lambda_i$, and $i = 1, 2$. Table 1 shows the patterns used in this study (*See* [59] for the entire collection). The proposed vector field classifier employs a continuous formulation given by

$$C(\lambda_1, \lambda_2) = \begin{cases} rs, & \lambda_1 > \delta, \lambda_2 > \delta, \\ 0, & \text{otherwise,} \end{cases} \qquad (1)$$

where δ is a threshold to exclude ill-conditioned matrices characterized by small eigenvalues, $r = \frac{min(|\lambda_1|, |\lambda_2|)}{max(|\lambda_1|, |\lambda_2|)}$ and $s = \frac{sign(\lambda_1, \lambda_2) + 1}{2}$. The term r includes converging or diverging configurations, i.e., attracting and repelling stars, as well as strong attracting and repelling nodes, such that $C(\lambda_1, \lambda_2) \approx 1$ (*See* Table 1) [59].

Therefore, the PPA returns the location of the converging configurations; one of which points to the OD. The PPA algorithm is explained below

Fig. 2 Mahfouz vectors: (top left) original image, (topright) the greatest difference of the number of pixels in the vertical and horizontal edges, (bottom left) y-location vs. the maximum number of bright pixels in a reference square at the x-location, (bottom right) the Mahfouz vectors
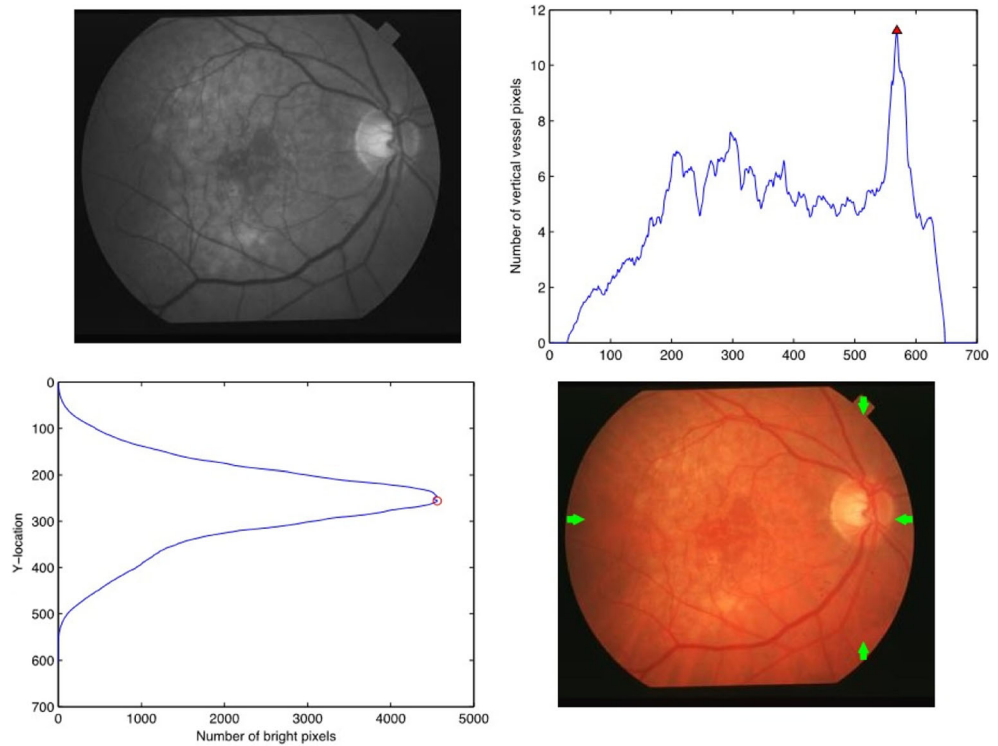
1) Input: SLBV, MV, BV, and SVV
2) Collect the SLBV, MV, BV, and SVV in a joint vector field.
3) Interpolate the vector field for every point of the image.
4) Using classifier (1) evaluate the PPA score for every point and create the PPA image.
5) Threshold the PPA image and find PPA regions.
6) Find a final PPA region using the maximum likelihood estimation based on: mean thickness of the segmented vessels, the contrast of segmented vessels compared to the background, the density of segmented vessels, and the PPA score.
7) Find the centroid of the final PPA region.

8) Validate the direction of the SVV: if the SVV points opposite to the direction to the centroid, flip the vector and recalculate the PPA image. Repeat for every SVV.
9) Output: the PPA region, the centroid of the PPA region.

Figure 3 illustrates the PPA techniques.

2.1.2 Hybrid method

An enhanced version of VVPPA is called the HM. The HM combines the VT proposed in [56] and VVPPA. The VT approximates the location of the OD by finding a centroid of a collection of points, of which the total sum of the distances

Table 1 Phase portrait analysis of a 2D vector flow

Pattern	Eigenvalues		Illustration
Saddle Point	$R_1 > 0, R_2 < 0$	$I_1 = I_2 = 0$	
Repelling Node	$R_1 \neq R_2 > 0$	$I_1 = I_2 = 0$	
Attracting Node	$R_1 \neq R_2 < 0$	$I_1 = I_2 = 0$	
Repelling Star	$R_1 = R_2 > 0$	$I_1 = I_2 = 0$	
Attracting Star	$R_1 = R_2 < 0$	$I_1 = I_2 = 0$	
Saddle node (edge)	$R_1 = 0, R_2 \neq 0$	$I_1 = I_2 = 0$	

Fig. 3 VVPPA algorithm: (top left) initial vectors SLBV (black), MV (gray), and BV (white), (top right) corresponding PPA from the initial vectors, (middle left) the first SVV, (middle right) after the direction correction of the first SVV, (bottom left) interpolated vector field and the corresponding PPA, (bottom right) centroid (rectangle), PPA boundary (dashed line), and the ground truth boundary (black line)
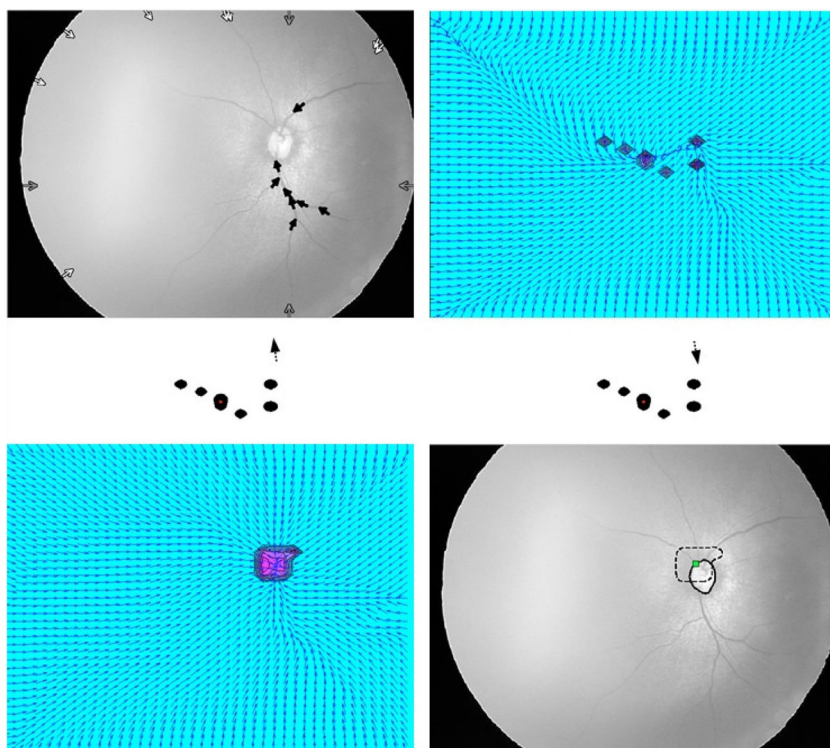
from each point in this collection to all vessel clusters is minimal. This HM aims to carry out the best accuracy of the VT and VVPPA. To localize OD, the HM creates a decision model to select an appropriate approach (VT or VVPPA). The decision is based on the number of bifurcation vectors, the number of SVV, and the PPA score. On the most basic level, the model switches to VT, if the number of basic vectors is not sufficient to conduct an appropriate PPA.

As the HM builds the model from the both approaches, its performance on a series of images is usually better than VT or VVPPA applied independently. Further, the HM reduces the computational time to approximately 50% relative to each individual approach.

2.2 Scale space algorithm with VVPPA/HM for OD segmentation

The scale space (SS) theory was originally proposed by Witkin [60] to create a multi-scale representation of signals in 1D. Lindeberg [61] applied the SS to image segmentation. The SS theory was applied by Duanggate et al. [57] for OD segmentation in the retinal images. In their work, a series of images

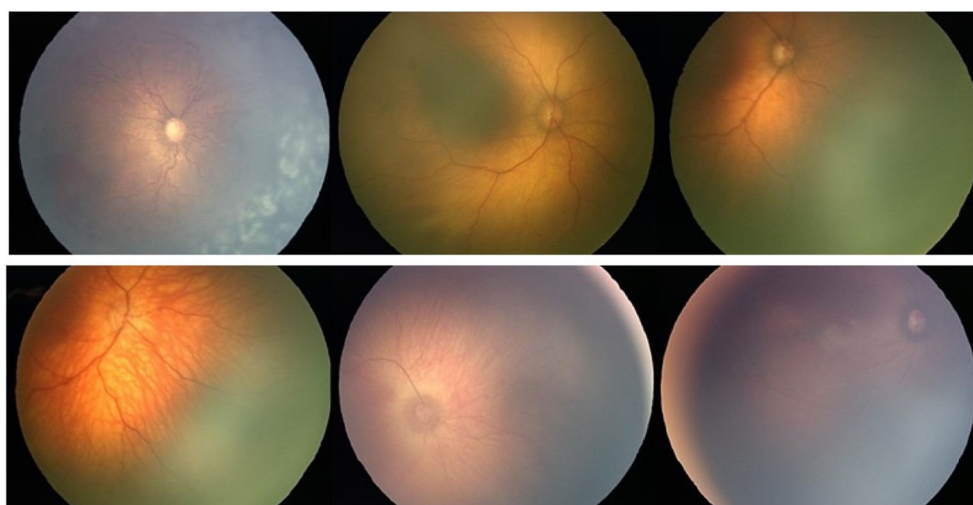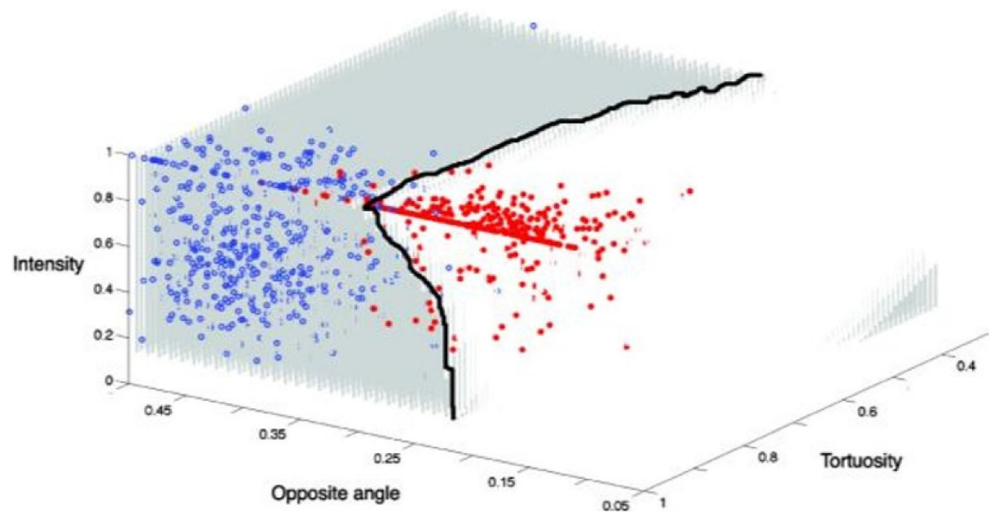Fig. 4 Examples of fair images (top) and poor images (bottom)

Fig. 5 The SVM decision model: dots—feature values of leading vectors, circles—feature values the non-leading vectors


resulting from applying the Gaussian blurring was constructed. The blobs (closed contours) extracted from the blurred images were linked and represented as a scale-space blob tree. Merging is applied to the blobs that meet the criteria of adjacency and stability. The OD is selected from these candidate blobs based on the size, entropy, intensity, and compactness. We integrate the SS scheme with VVPPA and with HM. In the framework of the SSVVPPA approach, the SS is modified by employing the PPA score along with the original features used in Duanggate's work. For the SSHM approach, the SS theory is combined with either the VT [56] or VVPPA. The choice of method to be combined with SSC depends on the decision returned by the HM. If the HM returns VT, the VT score is considered together with the original features used by the SS. As the boundary of the OD

blobs obtained from SS can be wavy, we approximate it by the best-fit circle (SSC).

2.3 Numerical experiments

We consider a standard database STructured Analysis of the REtina (STARE) [43]. The fundus photographs from STARE were captured by a TopCon TRV-50 fundus camera with 35° field of view. Each image was digitized to create a 605×700 pixels at 24 bits per pixel. Another dataset is collected to detect retinopathy of prematurity (ROP) by Prof. Sarah Barman with Kingston University of UK. All digital images from ROP were taken from patients with non-dilated pupils using a KOWA-7 non-mydriatic retinal camera with a 45° field of view.

Fig. 6 SSVVPPAC decision trees: (left) the ROP collection, (right) the STARE collection
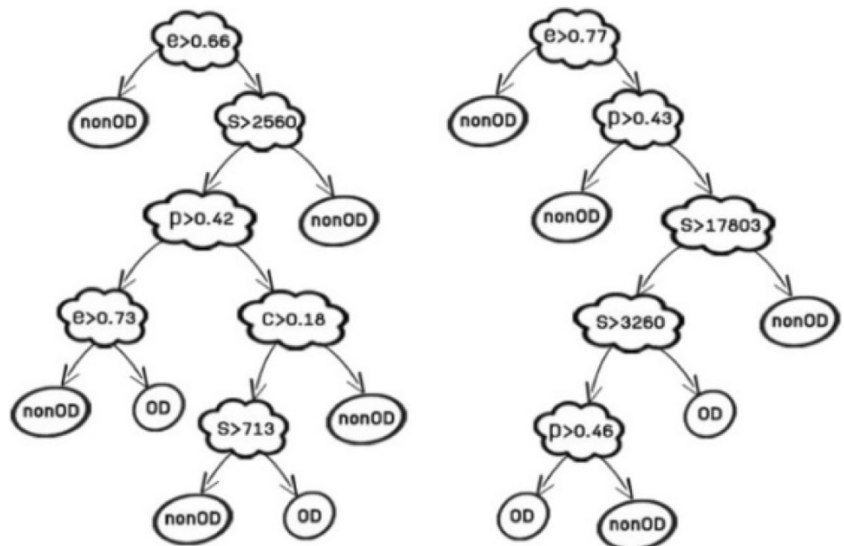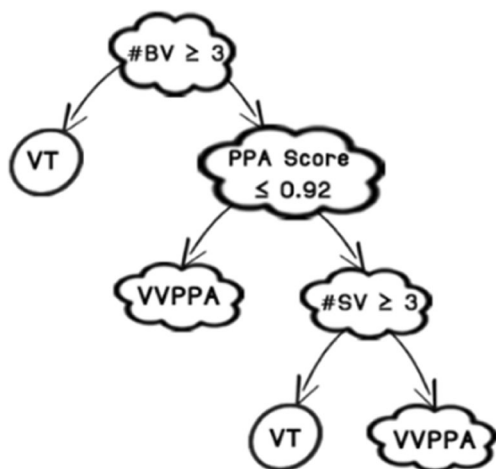
Fig. 7 The decision tree of the HM for OD localization (STARE and ROP)

The images were stored in JPEG format, 640 × 480 pixels at 24 bits per pixel. We classify images into two categories. The bright, round, and clear ODs are classified visually as fair. The rest is considered poor.

There are 91 images in the ROP collection with an average OD diameter of 47.9 pixels. Sixty images are classified as fair

and 31 as poor. STARE includes 81 images with an average OD diameter of 103.9. There are 31 images of fair quality and 50 images of poor quality. Examples of fair and poor retinal fundus images are displayed in Fig. 4.

To evaluate the proposed methods, hand-drawn ground truth (GT) images were obtained from human experts. To minimize the human expert bias, the GTs were obtained from three ophthalmologists from Thammasat University Hospital. Each ophthalmologist hand-drew the OD contour on each retina image from the two collections three times. The inter-observer variability is 0.86 and 0.91 for the ROP and STARE collections, respectively. The intra-observer variability is 0.91 and 0.93 for the ROP and STARE collections, respectively.

Since the two collections of the test images have been obtained by different devices with different illumination conditions, they require different decision models for leading vector classifications.

We employ an SVM classifier with the Gaussian kernel [62] trained using the standard 70–30% ratio between the training and the testing data. An example of the decision models for leading vector classification is shown in Fig. 5, where dots and circles represent the feature values of the leading and non-leading vectors, respectively. The axes represent the normalized

Fig. 8 Examples of the OD location results: GT—black solid line, FC—light gray circle, CTL—dark gray square, VT—gray triangle, VVPPA—black diamond, HM—white hexagon
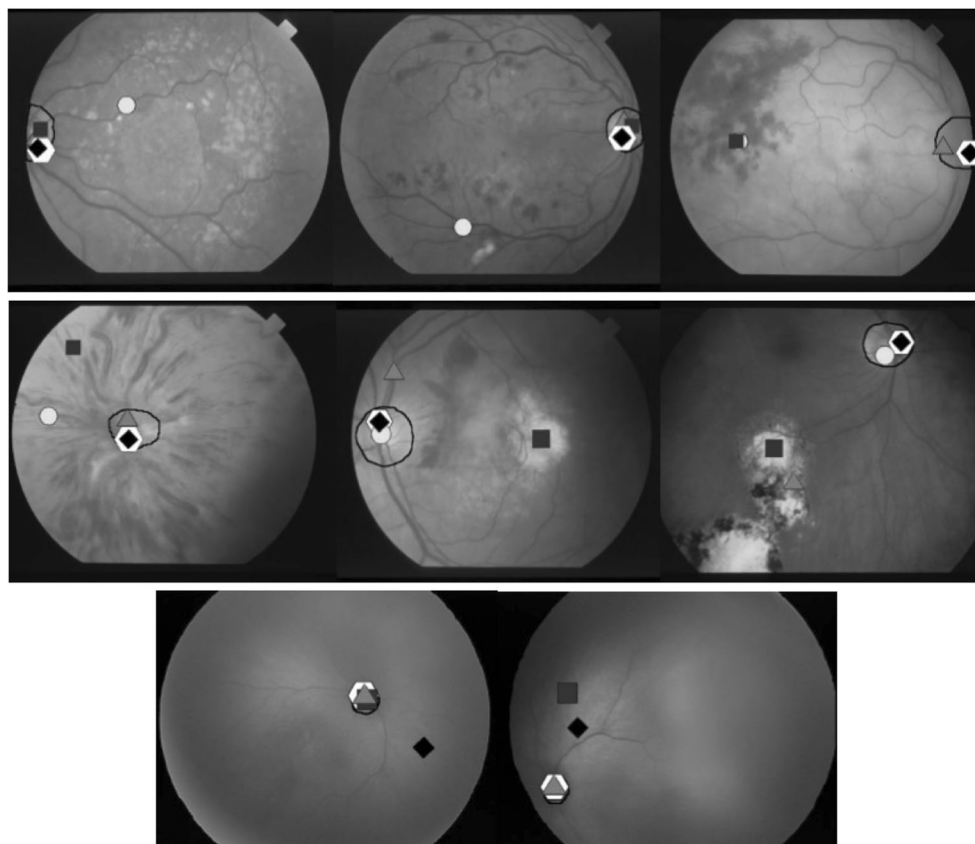
Table 2 Accuracy of the OD localization using FC, CTL, and VT vs. VVPPA and HM, in percent

Collections	ROP		STARE		Overall average	Overall average, fair	Overall average, poor
Image quality/method	Fair	Poor	Fair	Poor			
FC	N/A	N/A	90.32	88.00	N/A	N/A	N/A
CTL	88.33	64.52	100.00	98.00	87.71	94.16	81.26
VT	95.00	96.77	96.77	94.00	95.64	95.88	95.38
VVPPA	100.00	83.87	100.00	96.00	94.97	100.00	89.93
HM	100.00	96.77	100.00	98.00	98.69	100.00	97.38

values of three features: the opposite angle, the tortuosity, and the intensity. The black line indicates the decision boundary. The accuracy of the SVM model on the testing set is 96.61 and 94.11% for ROP and STARE, respectively.

In order to classify the candidate blobs produced by the SS procedure into the OD and non-OD groups, we use the automatic decision tree generator available from the Waikato Environment for Knowledge Analysis [40]. The 70/30 ratio was used for the training and testing. The corresponding decision tree requires the following features: the PPA score, size, compactness, entropy, and intensity denoted by p, s, c, e, and i, respectively. The following decision trees shown in Fig. 6 are used for classification of the OD. The constructed decision trees reveal that all features except intensity are important in detecting the OD.

As far as the SSHMC is concerned, the decision model includes the number of SLBV, SVV vectors, and the PPA score (See Fig. 7).

Fig. 9 Examples of the OD segmentation: 1—GT, 2—SSVTC, 3—SSC, 4—CTL, 5—SSVVPPAC, 6—SSHMC
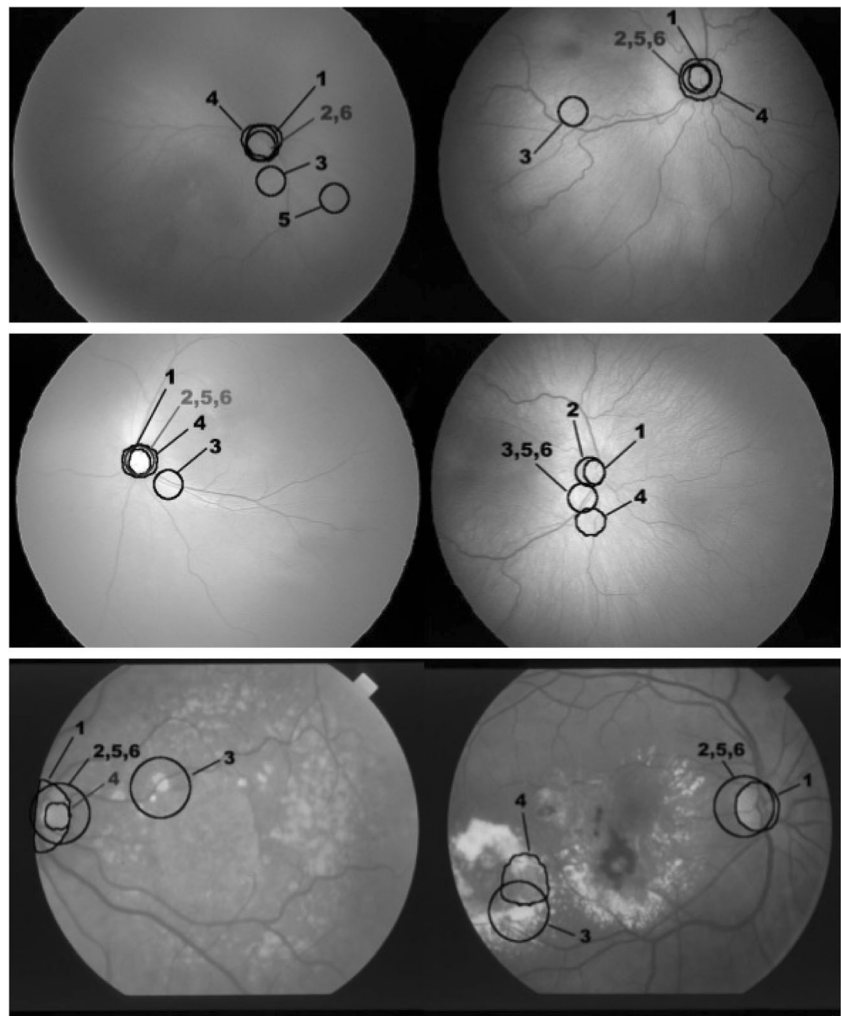
Table 3 The accuracy of the OD segmentation using CTL, SSC SSVTC, SSVVPPAC, and SSHMC, in percent

Evaluation	Methods	ROP		STARE		Overall average	Overall average, fair	Overall average, poor
		Fair	Poor	Fair	Poor			
Average sensitivity	CTL	74.29	61.28	72.59	41.23	62.35	73.44	51.26
	SSC	87.74	51.38	65.62	49.86	63.65	76.68	50.26
	SSVTC	89.60	80.07	76.14	59.97	76.45	82.87	70.02
	SSVVPPAC	89.60	72.72	75.30	59.94	74.39	82.45	66.33
	SSHMC	89.60	80.07	75.30	61.26	76.56	82.45	70.67
Average PPV	CTL	66.42	46.39	84.66	69.89	66.84	75.54	58.14
	SSC	80.56	49.84	62.19	57.54	62.53	71.38	53.69
	SSVTC	81.91	72.53	70.86	70.27	73.89	76.39	71.40
	SSVVPPAC	81.91	65.17	70.05	69.10	71.56	75.98	67.14
	SSHMC	81.91	72.53	70.05	71.08	73.89	75.98	71.81

3 Results

In this section, we test VVPPA and the HM against the FC method [4], a recent modification of the CT proposed by Lu (CTL) in [25] and our previous VT method [56]. For the OD segmentation, we compare the results of SSVVPPAC and SSHMC against the SSC, CTL, and SSVTC [41].

3.1 Performance of the VVPPA and HM in locating the OD

We test the VVPPA and HM against CTL method [25], FC method [4], and the VT method [56]. Figure 8 shows introductory examples of the OD location obtained by the VVPPA and HM vs. the three baseline approaches. VVPPA and HM generally perform better. The accuracy of OD localization is evaluated as follows. If the OD location is contained entirely inside the circle centered at the GT's centroid (the radius equals to the average GT radius of the collection), we considered this a correct result. The ratio of the correct cases to the total number of images yields the average accuracy. CTL is considered successful if the centroid of the CTL contour is located inside the GT contour.

The accuracy of the five competing OD localization methods tested against VVPPA and HM is shown in

Table 4 Computational time per image (≈400 × 400): CTL vs. the proposed method

| Percentage of test pixels (%)	No. of radial line segments	Average time: CTL (min)	Average time (min)		
			SSVTC	SSVVPPAC	SSHMC
20	40	1.57	4.85	2.55	2.85
20	180	6.63			
60	40	4.29			
60	180	18.84			

Table 2. The proposed approach outperforms CTL on both test collections and shows a better success rate against CTL by 7.26 and 10.98%, using VVPPA and HM, respectively. Even though VVPPA shows a reduction of accuracy against VT by 0.67%, the HM works better than VT with an absolute improvement of 3.05%. For all image collections differentiated by image quality, the absolute improvements of VVPPA and HM are noticeably better than CTL by 8.67 and 16.12%, respectively, for the poor sets and by 5.84 for the fair sets. When VVPPA and HM are compared to VT, they show an improvement in the fair sets by 4.12%. While the VVPPA success rate is lower than VT by 5.45%, the HM outperforms VT by 2.00% for the poor sets. Finally, among the tested methods, the HM yields the best performance in all categories.

3.2 Performance of SSVVPPAC and SSHMC

In this section, we present the results of the OD segmentation based on the SS algorithm and our OD localization approach along with the circular edge adjustment [57]. SSVVPPAC and SSHMC are compared with three OD segmentation methods: CTL, SSC, and SSVTC. Figure 9 shows the qualitative results of OD segmentation. The proposed method has been compared with the baseline methods in Table 3 in terms of the average sensitivity of all collections. The SSHMC provides an outstanding absolute improvement over CTL, SSC, and SSVTC by 14.21, 12.91, and 0.11%, respectively. For the average PPV, SSHMC shows an absolute improvement against CTL and SSC, respectively, by 7.05 and 11.36%, and approximately the same average PPV as SSVTC.

Furthermore, the proposed approach performs better for the fair quality sets in all collections, for both sensitivity and the PPV. The SSVVPPAC and SSHMC show the largest absolute improvement (sensitivity and PPV) for the fair set for the both collections by 9.01 and 0.44% against CTL, 5.77 and 4.61

Fig. 10 The HM approach fails: false OD (rectangle), GT (black line). **a** Insufficient vessel information. **b** Vessel-like artifacts
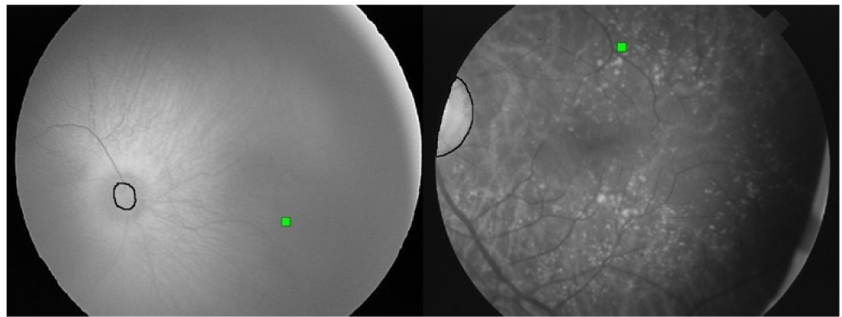
against SSC, and only a slight decrease by 0.42 and 0.41 against SSVTC.

For the poor quality sets, SSHMC shows a significant improvement in the sensitivity of 19.41, 20.05, and 0.64 when compared against CTL, SSC, and SSVTC, respectively. SSHMC yields a noticeably higher average PPV than CTL: its absolute improvement against CTL is 13.67%. The maximum average PPV of SSHMC has been also improved considerably by 18.12%.

Generally, the proposed approach outperforms SSC and CTL regardless of the quality of the images and for each data collection. In particular, when the image quality is poor, the proposed approach outperforms the other two methods substantially.

It should be noted that in [57], the SS method was found to be superior with regard to OD segmentations based on the morphological operations [22] and the circular Hough transform [63]. Moreover, in [25], Lu claims to outperform a genetic algorithm a direct search approach [29], a geometrical model of the vessel structure using two parabolas [35], a feature and vessel-based approach [64], and a morphologic two-stage approach [65]. Therefore, the proposed approach outperforms the abovementioned methods as well.

The SSHMC is a combination of VVPPA and VT designed to produce a better accuracy. The average improvement of SSVVPPAC and SSHMC on both collections against CTL method is, respectively, 12.04 and 14.21%, for the sensitivity, and 4.72 and 7.05%, for the PPV. In turn, the improvement produced by SSVVPPAC and SSHMC vs. SSC is, respectively, 10.74 and 12.91%, for the sensitivity, and 9.03 and 11.36%, for the PPV.

3.3 Computational time

Although the CTL method is claimed to be the fastest, its performance strongly depends on the threshold of the gray level (to select possible candidates for the center of the OD) and the number of radial segments used to verify the circularity of the object boundary. Lu also claims that the OD center always lies within the first 20% brightest pixels within the probability map of the OD. However, there are a number of poor quality images for which this is not correct. The increase of the above thresholds increases the computational time nonlinearly. For instance, changing the percentage of the brightest pixel threshold from 20 to 60% doubles the computational time, whereas changing the angular step from 6° to 2° increases the computational time of the CTL method by a factor of 10. Our method, programmed in MATLAB, requires on average of about 3-min processing on a standard database image 600 × 750 on a Dell computer with 3.30-GHz Intel Core i3 Processor with 4GB of random access memory. Table 4 shows the average computational time of SSVVPPAC and SSHMC against CTL and SSVTC. Furthermore, SSVVPPAC and HM are twice as fast as the VT approach, which is about 2 min per image.

3.4 Possible errors

Usually, an incorrect location of the OD produced by VVPPA is due to insufficient vessel information, for instance, when the resulting vector field comprises only one or two leading vectors (Fig. 10, left). Another cause is the presence of vessel-like artifacts such as shadows, lesions, and/or uneven illumination.

Fig. 11 Retinal images are taken using a portable retinal lens attached to an iPhone 6s

Fig. 12 A comparison of the quality of retina images taken from a standard fundus microscope (left) and an IPhone 6s camera with a portable lens (right)
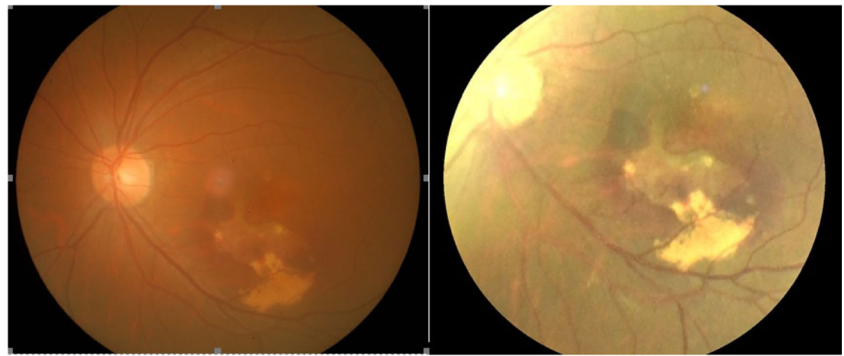
The artifacts can produce incorrect leading vectors and generate a false OD (Fig. 10, right)

When the case of insufficient vessel information is detected, the user is suggested to use other approaches employing standard OD features.

4 Clinical application

The proposed HM can be used as a post-processing algorithm on the top of any segmentation method as long as the segmentation procedure offers multiple candidates for the OD. Methods such as a basic thresholding, adaptive thresholding, watershed segmentation, clustering, and region growing can be integrated with the HM. Furthermore, the HM can be applied to generate seeds for such popular segmentation routines as region growing, active contours, and the level set method.

Our clinical application includes 182 retinal images obtained from the Eye Center of Thammasat University Hospital of Bangkok. This government hospital provides relatively inexpensive or even free of charge service. However, the long waiting time before the examination and consultation with the doctor often deters patients from using the service. This is especially important in the case of DR since many patients are not aware of their condition. Even when the DR-related retinal exudates start to leak, the patient's vision is not seriously affected because the locations of the exudates could be far away from the fovea. According to the WHO, only half of

Fig. 13 Clinical application: (top left) retinal image produced by a smartphone, (top right) vector field and the PPA image, (bottom left) candidate exudates, (bottom right) the OD has been eliminated; the image is classified as normal
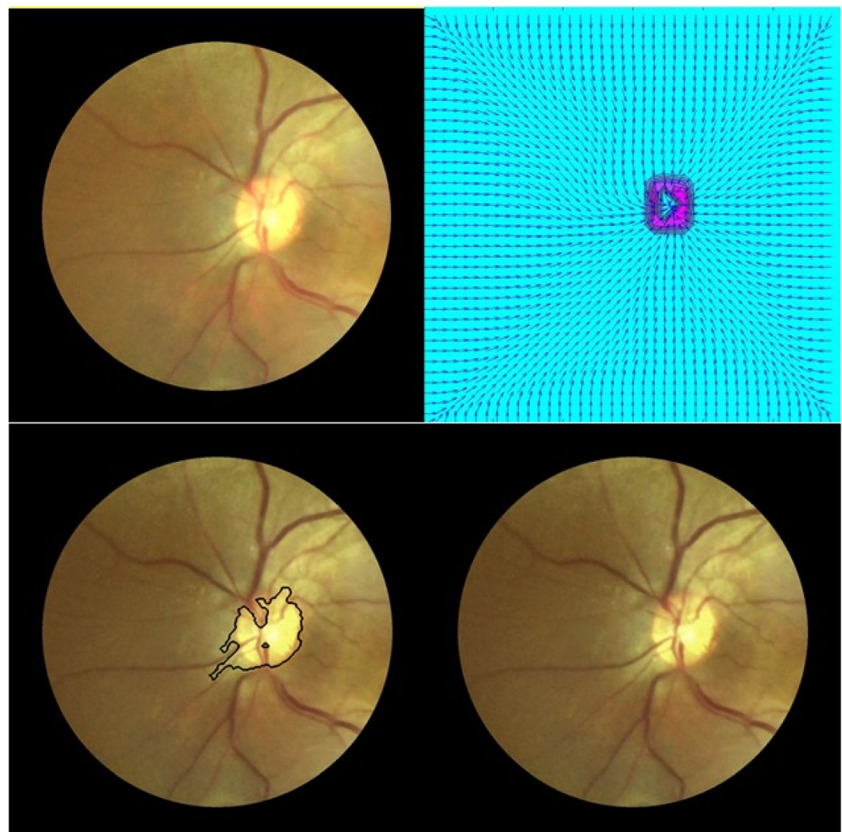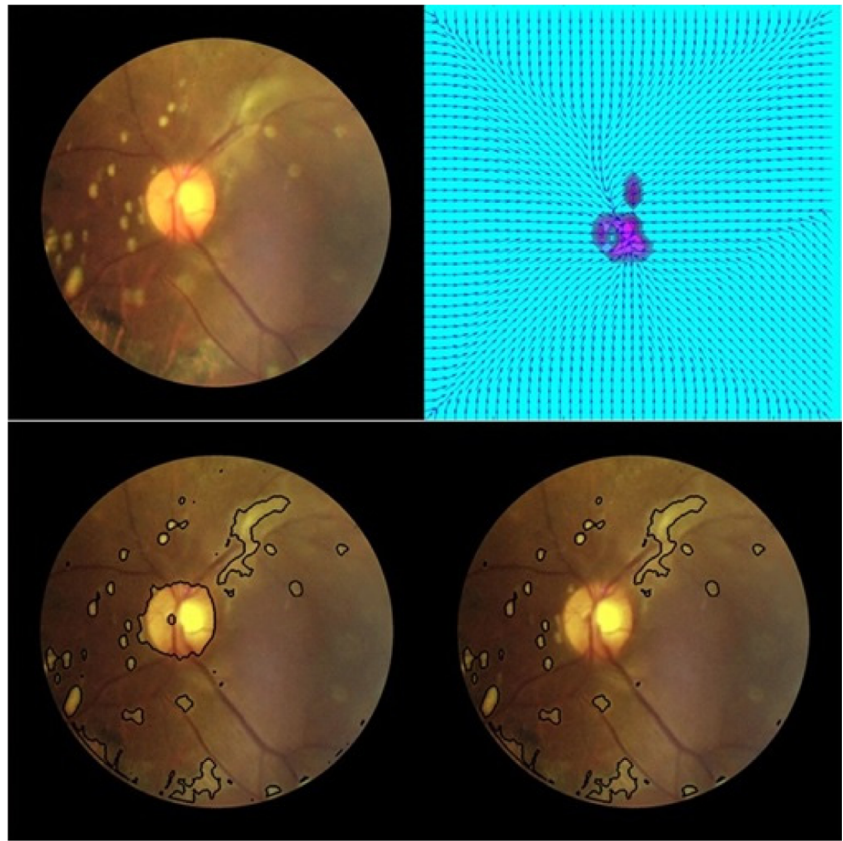
Fig. 14 Clinical application: (top left) retinal image produced by a smartphone, (top right) vector field and the PPA image, (bottom left) candidate exudates, (bottom right) the OD has been eliminated; the image is classified as abnormal

the patients are aware of the disease. As far as the health care in Thailand is concerned, in 2014, Thailand had only 1080 ophthalmologists nationwide; 75% of which worked at big hospitals in Bangkok and nearby provinces. Therefore, the majority of the DR in the rural areas remains untreated until the damage is irreversible or requires a high cost treatment.

Our clinical scenario is that the images are taken by an inexpensive portable lens connected to a smart phone by a qualified nurse prior or even instead of a visit to the doctor. In the real clinical experiment, the images were processed immediately by a relevant software which excludes the OD, using the proposed technique, and detects abnormalities related to DR using a combination of an adaptive thresholding with regard to the image intensity [66] and the HM (See Fig. 11). The signs of DR include exudates (leakage of protein from the vessels) and cotton-wool spots (nerve fiber layer infarctions). The classification criterion is very simple, when the image has at least one region of exudates, it is considered to be abnormal.

Next, the patient is examined by a conventional retinal imaging system and the diagnosis made by the doctor is compared with that made by the software. All images are anonymous. The experiments have received an official ethical clearance from the National Medical Counsel of Thailand. The portable lens from Volk Optical Inc. [67] was connected to an iPhone 6s (8-megapixel camera). The lens is characterized

by the static view of 50% and the dynamic view of 80%. The images were automatically sent to a Google Drive from which they were processed and classified. For simplicity, we consider only two classes: a healthy retina and a retina with abnormalities. A generalization to various staging of DR is a future work based on classification methods [66, 68–70].

It should be noted that the quality of retinal images obtained by the compact lens is in general poorer than that produced by a standard fundus microscope (See Fig. 12). As a matter of fact, classification of retinal images obtained by various compact cameras attached to a smart phone represents a standalone interesting practical problem being discussed in the ophthalmology community for quite some time [71–75].

Clearly, the portable lens image is characterized by an increased blur, artifacts, and reflections. Besides, the vascular system is often incomplete due to the fact that the lens has narrower field of view compared to that from a standard fundus microscope. However, our experiments demonstrate that

Table 5 Accuracy of the classification of the smartphone images using the proposed method

True positive	True negative	False positive	False negative
98.13%	94.67%	5.33%	1.87%

the proposed HM integrated with a very basic segmentation technique makes it possible to successfully eliminate the OD and perform correct classification. Figures 13 and 14 illustrate the proposed approach.

Finally, Table 5 displays the classification results obtained using the HM applied to 182 smartphone images in the real clinical conditions.

5 Conclusions

A novel approach, based on a combination of VVPPA and VT, has been proposed and verified. VVPPA localizes the OD by detecting vessels pointing out to the OD at bifurcation points and analyzing the resulting vector field by PPA. The vessels at the bifurcation points are classified by SVM using a set of appropriate features. The leading vectors have been complemented the MV and synthesized BV created to ensure the convergence to the OD.

The HM applies a decision tree to decide whether VT or VVPPA should be used. Furthermore, to obtain the OD boundary, the HM is integrated into a SS segmentation algorithm. This integration generates new SS-based methods called SVVPPAC and SSHMC. The PPA score obtained from VVPPA is used as an additional feature by the SS approach [57]. In turn, the HM incorporates either VT or VVPPA features selected by the corresponding decision tree.

The numerical experiments on OD localization (two databases, 172 images) demonstrate that the proposed approach outperforms the existing methods considerably. The HM yields the highest results: 100% accuracy for fair quality and 97.38% for poor quality images.

As far as the segmentation algorithms are concerned, SSHMC and SSCVVPA on average outperform the benchmark methods. SSVVPPAC and SSHMC yield the highest PPV and sensitivity. SSHMC and SSVVPPAC achieve up of 82.45% sensitivity on the fair set of images. Furthermore, the HM obtains the highest sensitivity of 70.67% for the poor set of images. The proposed algorithm also outperforms CTL, which previously was claimed to be the best, in terms of computational time.

Finally, the proposed HM has been applied in the real clinical environment to prove the possibility of using the portable smartphone lens and the proposed method to differentiate the normal and abnormal retinal images prior to an examination by the standard equipment. The experiments demonstrate that the true positive measure is close to 100%, whereas the true negative is 94.67%.

References

1. Bourne RR, Sukudom P, Foster PJ, Tantisevi V, Jitapunkul S, Lee PS, Johnson GJ, Rojanapongpun P (2003) Prevalence of glaucoma in Thailand: a population based survey in Rom Klao District, Bangkok. Br J Ophthalmol 87:1069–1074

2. World Health Organization (2016) WHO|Diabetes. In: fact sheet of WHO Media Centre. http://www.who.int/mediacentre/factsheets/fs312/ en/. Accessed 30 July 2016

3. MacGillivray TJ, Trucco E, Cameron JR, Dhillon B, Houston JG, van Beek EJ (2014) Retinal imaging as a source of biomarkers for diagnosis, characterization and prognosis of chronic illness or long-term conditions. Br J Radiol 87:20130832. doi:10.1259/bjr.20130832

4. Hoover A, Goldbaum M (2003) Locating the optic nerve in a retinal image using the fuzzy convergence of the blood vessels. IEEE Trans Med Imaging 22:951–958

5. Li H, Chutatape O (2004) Automated feature extraction in color retinal images by a model based approach. IEEE Trans Biomed Eng 51:246–254

6. Lalonde M, Beaulieu M, Gagnon L (2001) Fast and robust optic disc detection using pyramidal decomposition and Hausdorff-based template matching. IEEE Trans Med Imaging 20:1193–1200

7. Dehghani A, Moghaddam HA, Moin M-S (2012) Optic disc localization in retinal images using histogram matching. EURASIP J Image Video Proc 2012:1–11. doi:10.1186/1687-5281-2012-19

8. Lowell J, Hunter A, Steel D, Basu A, Ryder R, Fletcher E, Kennedy L (2004) Optic nerve head segmentation. IEEE Trans Med Imaging 23:256–264

9. Winder RJ, Morrow PJ, McRitchie IN, Bailie JR, Hart PM (2009) Algorithms for digital image processing in diabetic retinopathy. Comput Med Imaging Graph 33:608–622

10. Li H, Chutatape O (2003) A model-based approach for automated feature extraction in fundus images. In: Ninth IEEE International Conference on Computer Vision, Nice, France. pp 394–399

11. Li H, Chutatape O (2003) Boundary detection of optic disk by a modified ASM method. Pattern Recogn 36:2093–2104

12. Morales S, Naranjo V, Angulo U, Alcaniz M (2013) Automatic detection of optic disc based on PCA and mathematical morphology. IEEE Trans Med Imaging 32:786–796

13. Hsiao H-K, Liu C-C, Yu C-Y, Kuo S-W, Yu S-S (2012) A novel optic disc detection scheme on retinal images. Expert Syst Appl 39:10600–10606

14. Sinthanayothin C, Boyce J, Cook H, Williamson T (1999) Automated localisation of the optic disc, fovea, and retinal blood vessels from digital colour fundus images. Br J Ophthalmol 83:902–910

15. Akram UM, Khan SA (2012) Automated detection of dark and bright lesions in retinal images for early detection of diabetic retinopathy. J Med Syst 36:3151–3162

16. Lu S, Liu J, Lim JH, Zhang Z, Tan NM, Wong WK, Li H, Wong TY (2010) Automatic optic disc segmentation based on image brightness and contrast. Proc SPIE 7623:76234J-76234J-8. doi:10.1117/12.844654

17. Esmaeili M, Rabbani H, Dehnavi AM, Dehghani A (2012) Automatic detection of exudates and optic disk in retinal images using curvelet transform. IET Image Process 6:1005–1013

18. Esmaeili M, Rabbani H, Dehnavi AM (2012) Automatic optic disk boundary extraction by the use of curvelet transform and deformable variational level set model. Pattern Recogn 45:2832–2842

19. Shahbeig S, Pourghassem H (2013) Fast and automatic algorithm for optic disc extraction in retinal images using principle-component-analysis-based preprocessing and curvelet transform. J Opt Soc Am A Opt Image Sci Vis 30:13–21

20. Pereira C, Goncalves L, Ferreira M (2013) Optic disc detection in color fundus images using ant colony optimization. Med Biol Eng Comput 51:295–303

21. Ramakanth SA, Babu RV (2014) Approximate nearest neighbour field based optic disk detection. Comput Med Imaging Graph 38: 49–56

22. Sopharak A, Uyyanonvara B, Barman S, Williamson TH (2008) Automatic detection of diabetic retinopathy exudates from non-dilated retinal images using mathematical morphology methods. Comput Med Imaging Graph 32:720–727

23. Azuara-Blanco A, Harris A, Cantor L, Abreu M, Weinland M (1998) Effects of short term increase of intraocular pressure on optic disc cupping. Br J Ophthalmol 82:880–883

24. Zhu X, Rangayyan RM, Ells AL (2010) Detection of the optic nerve head in fundus images of the retina using the Hough transform for circles. J Digit Imaging 23:332–341

25. Lu S (2011) Accurate and efficient optic disc detection and segmentation by a circular transformation. IEEE Trans Med Imaging 30: 2126–2133

26. Welfer D, Scharcanski J, Kitamura CM, Dal Pizzol MM, Ludwig LW, Marinho DR (2010) Segmentation of the optic disk in color eye fundus images using an adaptive morphological approach. Comput Biol Med 40:124–137

27. Youssif AR, Ghalwash AZ, Ghoneim AR (2008) Optic disc detection from normalized digital fundus images by means of a vessels' direction matched filter. IEEE Trans Med Imaging 27:11–18

28. Mahfouz AE, Fahmy AS (2010) Fast localization of the optic disc using projection of image features. IEEE Trans Image Process 19: 3285–3289

29. Carmona EJ, Rincon M, Garcia-Feijoo J, Martinez-de-la-Casa JM (2008) Identification of the optic nerve head with genetic algorithms. Artif Intell Med 43:243–259

30. Giachetti A, Ballerini L, Trucco E (2014) Accurate and reliable segmentation of the optic disc in digital fundus images. J Med Image 1:024001. doi:10.1117/1.JMI.1.2.024001

31. Aquino A, Gegúndez ME, Marín D (2010) Automated optic disc detection in retinal images of patients with diabetic retinopathy and risk of macular edema. Int J Biol Life Sci 8:353–358

32. Akita K, Kuga H (1982) A computer method of understanding ocular fundus images. Pattern Recogn 15:431–443

33. Chrástek R, Skokan M, Kubecka L, Wolf M, Donath K, Jan J, Michelson G, Niemann H (2004) Multimodal retinal image registration for optic disk segmentation. Methods Inf Med 43:336–342

34. Kavitha D, Shenbaga Devi S (2005) Automatic detection of optic disc and exudates in retinal images. In: IEEE Proceedings of 2005 International Conference on Intelligent Sensing and Information Processing, Chennai. pp 501–506

35. Foracchia M, Grisan E, Ruggeri A (2004) Detection of optic disc in retinal images by means of a geometrical model of vessel structure. IEEE Trans Med Imaging 23:1189–1195

36. Niemeijer M, Abramoff MD, van Ginneken B (2009) Fast detection of the optic disc and fovea in color fundus photographs. Med Image Anal 13:859–870

37. Dehghani A, Moin M-S, Saghafi M (2012) Localization of the optic disc center in retinal images based on the Harris corner detector. Biomed Eng Lett 2:198–206

38. Zhang D, Zhao Y (2016) Novel accurate and fast optic disc detection in retinal images with vessel distribution and directional characteristics. IEEE J Biomed Health Inform 20:333–342

39. Mendonca AM, Sousa A, Mendonca L, Campilho A (2013) Automatic localization of the optic disc by combining vascular and intensity information. Comput Med Imaging Graph 37:409–417

40. Semashko AS, Krylov AS, Rodin AS (2011) Using blood vessels location information in optic disk segmentation. In: Maino G, Foresti GL (eds) Image analysis and processing—ICIAP 2011. Springer, Berlin, pp 384–393

41. Rangayyan RM, Zhu X, Ayres FJ, Ells AL (2010) Detection of the optic nerve head in fundus images of the retina with Gabor filters and phase portrait analysis. J Digit Imaging 23:438–453

42. Staal J, Abramoff MD, Niemeijer M, Viergever MA, van Ginneken B (2004) Ridge-based vessel segmentation in color images of the retina. IEEE Trans Med Imaging 23:501–509

43. Hoover A, Goldbaum M (1975) The STructure Analysis of the REtina (STARE) project. http://www.ces.clemson.edu/~ahoover/stare. Accessed 18 Feb 2013

44. Alshayeji M, Al-Roomi SA, Abed S (2017) Optic disc detection in retinal fundus images using gravitational law-based edge detection. Med Biol Eng Comput 55:935–948

45. Rahebi J, Hardalaç F (2016) A new approach to optic disc detection in human retinal images using the firefly algorithm. Med Biol Eng Comput 54:453–461

46. Tan JH, Acharya UR, Bhandary SV, Chua KC, Sivaprasad S (2017) Segmentation of optic disc, fovea and retinal vasculature using a single convolutional neural network. J Comput Sci. doi:10.1016/j.jocs.2017.02.006

47. Harangi B, Hajdu A (2015) Detection of the optic disc in fundus images by combining probability models. Comput Biol Med 65: 10–24

48. Maity M, Das DK, Dhane DM, Chakraborty C, Maiti A (2016) Fusion of entropy-based thresholding and active contour model for detection of exudate and optic disc in color fundus images. J Med Biol Eng 36:795–809

49. Mary MCVS, Rajsingh EB, Jacob JKK, Anandhi D, Amato U, Selvan SE (2015) An empirical study on optic disc segmentation using an active contour model. Biomed Signal Process Control 18: 19–29

50. Wu X, Dai B, Bu W (2016) Optic disc localization using directional models. IEEE Trans Image Process 25:4433–4442

51. Xiong L, Li H (2016) An approach to locate optic disc in retinal images with pathological changes. Comput Med Imaging Graph 47:40–50

52. Díaz-Pernil D, Fondón I, Peña-Cantillana F, Gutiérrez-Naranjo MA (2016) Fully automatized parallel segmentation of the optic disc in retinal fundus images. Pattern Recogn Lett 83:99–107

53. Rodrigues LC, Marengoni M (2017) Segmentation of optic disc and blood vessels in retinal images using wavelets, mathematical morphology and Hessian-based multi-scale filtering. Biomed Signal Process Control 36:39–49

54. Bharkad S (2017) Automatic segmentation of optic disk in retinal images. Biomed Signal Process Control 31:483–498

55. Panda R, Puhan NB, Panda G (2017) Robust and accurate optic disk localization using vessel symmetry line measure in fundus images. Biocybern Biomed Eng 37:466–476

56. Muangnak N, Aimmanee P, Makhanov S, Uyyanonvara B (2015) Vessel transform for automatic optic disk detection in retinal images. IET Image Process 9:743–750

57. Duanggate C, Uyyanonvara B, Makhanov SS, Barman S, Williamson T (2011) Parameter-free optic disc detection. Comput Med Imaging Graph 35:51–63

58. Suykens JAK, Vandewalle J (1999) Least squares support vector machine classifiers. Neural Process Lett 9:293–300

59. Chucherd S, Rodtook A, Makhanov SS (2010) Phase portrait analysis for multiresolution generalized gradient vector flow. IEICE

Trans Inf Syst E93-D:2822–2835. doi:10.1587/transinf.E93.D.2822

60. Witkin A (1984) Scale-space filtering: a new approach to multi-scale description. In: ICASSP '84. IEEE International Conference on Acoustics, Speech, and Signal Processing, San Diego, pp 150–153

61. Lindeberg T (1994) Scale-space theory in computer vision. Springer US, US

62. Chang C-C, Lin C-J (2011) LIBSVM: a library for support vector machines. ACM Trans Intell Syst Technol 2:1–27. doi:10.1145/1961189.1961199

63. Sekhar S, Al-Nuaimy W, Nandi AK (2008) Automated localisation of retinal optic disk using Hough transform. In: 5th IEEE International Symposium on Biomedical Imaging: From Nano to Macro, Paris, pp 1577–1580

64. Ravishankar S, Jain A, Mittal A (2009) Automated feature extraction for early detection of diabetic retinopathy in fundus images. In: IEEE Conference on Computer Vision and Pattern Recognition, Miami, pp 210–217

65. Welfer D, Scharcanski J, Marinho DR (2013) A morphologic two-stage approach for automated optic disk detection in color eye fundus images. Pattern Recogn Lett 34:476–485

66. Akram MU, Tariq A, Khan SA, Javed MY (2014) Automated detection of exudates and macula for grading of diabetic macular edema. Comput Methods Prog Biomed 114:141–152

67. Volk (2016) Volk iNview retinal camera. In: Volk Optical Inc. https://volk.com/index.php/volk-products/ophthalmic-cameras/volk-inview.html. Accessed 30 July 2016

68. Ibrahim S, Chowriappa P, Dua S, Acharya UR, Noronha K, Bhandary S, Mugasa H (2015) Classification of diabetes maculopathy images using data-adaptive neuro-fuzzy inference classifier. Med Biol Eng Comput 53:1345–1360

69. Mookiah MR, Acharya UR, Chandran V, Martis RJ, Tan JH, Koh JE, Chua CK, Tong L, Laude A (2015) Application of higher-order spectra for automated grading of diabetic maculopathy. Med Biol Eng Comput 53:1319–1331

70. ter Haar Romeny BM, Bekkers EJ, Zhang J, Abbasi-Sureshjani S, Huang F, Duits R, Dashtbozorg B, Berendschot TTJM, Smit-Ockeloen I, Eppenhof KAJ, Feng J, Hannink J, Schouten J, Tong M, Wu H, van Triest HW, Zhu S, Chen D, He W, Xu L, Han P, Kang Y (2016) Brain-inspired algorithms for retinal image analysis. Mach Vis Appl 27:1117–1135

71. Abbas Q, Fondon I, Sarmiento A, Jiménez S, Alemany P (2017) Automatic recognition of severity level for diagnosis of diabetic retinopathy using deep visual features. Med Biol Eng Comput. doi:10.1007/s11517-017-1638-6

72. Prasanna P, Jain S, Bhagat N, Madabhushi A (2013) Decision support system for detection of diabetic retinopathy using smartphones. In: 7th International Conference on Pervasive Computing Technologies for Healthcare and Workshops. Venice 2013:176–179

73. Xu X, Ding W, Wang X, Cao R, Zhang M, Lv P, Xu F (2016) Smartphone-based accurate analysis of retinal vasculature towards point-of-care diagnostics. Sci Rep 6:34603. doi:10.1038/srep34603

74. Bastawrous A, Giardini ME, Bolster NM, Peto T, Shah N, Livingstone IA, Weiss HA, Hu S, Rono H, Kuper H, Burton M (2016) Clinical validation of a smartphone-based adapter for optic disc imaging in Kenya. JAMA Ophthalmol 134:151–158

75. Rajalakshmi R, Arulmalar S, Usha M, Prathiba V, Kareemuddin KS, Anjana RM, Mohan V (2015) Validation of smartphone based retinal photography for diabetic retinopathy screening. PLoS One 10:e0138285. doi:10.1371/journal.pone.0138285

Ms. Muangnak is a Ph.D. candidate at Thammasat University. She obtained her B.S. and M.S. in Computer Science. Her research areas are medical image processing and computer vision.

Dr. Aimmanee is an assistant professor at Thammasat University. Applied Mathematics is her background. She curently researches in the areas of information retrieval and medical image processing.

Dr. Makhanov is a full professor at Thammasat University of Bangkok. His MS and Ph.D. degrees are in applied mathematics. His research areas are robotics, image processing, and pattern recognition.